

## Reconciled Nanoarchitecture with Overlapped 2D Anatomy for High-Energy Hybrid Supercapacitors

Salah Abureden, Fathy M. Hassan, Aiping Yu, and Zhongwei Chen\*[a]

A unique and novel, flower bouquet-like, vanadium disulfide ( $\text{VS}_2$ ) nanosheet structure with very small prominent  $\text{VS}_2$  nanoparticles (10–25 nm) anchored on the surface of graphene nanosheets ( $\text{VS}_2/\text{G}$ ) was synthesized by a facile solvothermal method. The material showed superior electrochemical performance upon testing as a supercapacitor and achieved specific capacitance values of 211 and 135  $\text{F g}^{-1}$  at current densities of 1 and 20  $\text{A g}^{-1}$ , respectively, with 97% capacitance retention after 8000 cycles at 5  $\text{A g}^{-1}$  with high coulombic efficiency. The material was used to fabricate a full-cell hybrid supercapacitor (HSC), which showed a specific capacitance of 132  $\text{F g}^{-1}$  at a current density of 1  $\text{A g}^{-1}$  with remarkable cyclability up to 8000 cycles at 5  $\text{A g}^{-1}$  and a loss of less than  $1 \times 10^{-4} \text{ F cycle}^{-1}$ . The HSC demonstrated an excellent energy density of 46.93  $\text{Wh kg}^{-1}$  at a power density of 0.91  $\text{kW kg}^{-1}$  and retained a high energy density of 23.11  $\text{Wh kg}^{-1}$  even upon increasing the power density tenfold (9.40  $\text{kW kg}^{-1}$ ). This unique material synthesized by a simple method is a very promising candidate for next-generation energy-storage technologies that can fill the gap between batteries and supercapacitor devices.

The global energy challenges and the increasing demand for reliable and cost-effective energy-storage and energy-conversion devices have inspired researchers to explore new materials to meet the growing demands.<sup>[1]</sup> Lithium-ion batteries (LIBs) are one kind of energy storage device; they are based on faradic reactions and are capable of delivering high energy densities with limited power densities.<sup>[2]</sup> On the other hand, supercapacitors are another kind of energy-storage device; they are based on the electrical double-layer capacitor (EDLC) storage mechanism and can deliver high power densities with limited energy densities.<sup>[3]</sup> The idea of creating a hybrid device that can combine the characteristics of both batteries and supercapacitors has attracted the attention of researchers in the last decade. Researchers have investigated different materials for the faradic part of hybrid supercapacitor (HSCs), including metal oxides such as  $\text{RuO}_2$ ,<sup>[4]</sup>  $\text{MnO}_2$ ,<sup>[5]</sup>  $\text{Li}_4\text{Ti}_5\text{O}_{12}$ ,<sup>[6]</sup>  $\text{V}_2\text{O}_5$ ,<sup>[7]</sup> and  $\text{Co}_2\text{O}_3$ ,<sup>[8]</sup> metal sulfides such as  $\text{MoS}_2$ ,<sup>[9]</sup> and  $\text{NiCo}_2\text{S}_4$ ,<sup>[10]</sup> and conducting polymers such as

polyaniline<sup>[11]</sup> and polypyrrole.<sup>[12]</sup> However, despite recent success in improving the energy density of HSCs, low power densities and limited cycle life are still challenging factors in the energy-demanding applications of hybrid supercapacitors.<sup>[13]</sup>

These changes can be met by the following strategies:

- 1) The use of a highly conductive substrate such as graphene can enhance charge-transfer kinetics, which should lead to increased stability at higher power rates<sup>[1c,14]</sup>
- 2) The use of advanced morphologies that can provide wide contact with an electrolyte-like sheet structure can increase the number of electroactive sites with short diffusion paths<sup>[15]</sup>
- 3) The growth of nanosize particles on the surface of the sheet structure can enhance the stability of the material and provide additional electroactive sites<sup>[16]</sup>

The combination of all three of these strategies together can lead to an increase in the energy density without a significant loss of power density.

One of the materials that can combine these strategies together is vanadium disulfide, which is a type of layered transition-metal dichalcogenide (TMD); it has great potential in hybrid supercapacitor devices because of its excellent conductivity, distinctive nanosheet structure, and high ion-diffusion kinetics.<sup>[9b,17]</sup> The advantages of using vanadium disulfide over traditional carbon materials include: one, the ability to provide high energy density at high power rates; two, the ability to provide additional pseudocapacitance through faradic redox reactions. However, the synthesis of vanadium disulfide is difficult and requires the use of a  $\text{H}_2\text{S}$  atmosphere and high temperatures, and these factors have limited the interest of researchers in investigating the potential of  $\text{VS}_2$  in supercapacitor applications.<sup>[18]</sup> Only two reports have successfully investigated the use of  $\text{VS}_2$  in supercapacitor applications by using simple synthesis methods. Feng et al.<sup>[18a]</sup> reported the synthesis of few-layers  $\text{VS}_2$  nanosheets by using an all-in-solution route in a hydrothermal reaction. The synthesized  $\text{VS}_2$  showed high conductivity and a considerable specific capacitance of 4760  $\mu\text{F cm}^{-2}$ . Masikhwa et al.<sup>[19]</sup> reported the use of a hydrothermal reaction to synthesize  $\text{VS}_2$  nanosheets, which were used for the first time in the fabrication of an asymmetric supercapacitor showing a specific capacitance of 155  $\text{F g}^{-1}$  and an energy density of 42  $\text{Wh Kg}^{-1}$  at a power density of 0.70  $\text{kW kg}^{-1}$ .

On the other hand, the superior electrical and mechanical characteristics of graphene in addition to its large surface area have motivated an enormous number of researchers to investigate its uses in electrochemical devices.

[a] S. Abureden, Dr. F. M. Hassan, Prof. A. Yu, Prof. Z. Chen  
Chemical Engineering Department  
University of Waterloo  
200 University Ave.  
Waterloo, Ontario, N2L 3G1 (Canada)  
E-mail: zhwen@uwaterloo.ca

Supporting Information and the ORCID identification number(s) for the author(s) of this article can be found under <https://doi.org/10.1002/ente.201700225>.

To the best of our knowledge, there are no reports in the literature on the use of  $\text{VS}_2$  on graphene ( $\text{VS}_2/\text{G}$ ) in a HSC. We herein report, for the first time, a facile, inexpensive, and scalable synthesis of a unique  $\text{VS}_2$  nanosheet flower bouquet-like structure with  $\text{VS}_2$  nanoparticles attached to it and anchored onto the surface of graphene nanosheets by using a solvothermal method (Figure S1 in the Supporting Information) without the need to use toxic materials such as  $\text{H}_2\text{S}$ , which is usually used to synthesize  $\text{VS}_2$ .<sup>[18,20]</sup> The developed morphology provides a wide contact area with the electrolyte, a large number of electroactive sites, short diffusion paths, high stability, and fast charge-transfer kinetics. The material shows superior electrochemical performance for supercapacitor applications and is able to achieve a specific capacitance of  $211 \text{ F g}^{-1}$  at a current density of  $1 \text{ A g}^{-1}$  and maintains a high capacitance of  $135 \text{ F g}^{-1}$  even if the current density is increased to  $20 \text{ A g}^{-1}$ . Moreover, the material shows 97% capacitance retention after 8000 cycles and thus has high potential in HSC applications, which opens the door for more investigation into its possible uses. For better understanding of the interaction of sulfur with graphene oxide, we synthesized sulfur-doped graphene (SG) by using the same experimental procedure as that outlined for  $\text{VS}_2/\text{G}$ , as discussed in the Supporting Information.

The structure and morphology characteristics were examined by a number of techniques, including X-ray diffraction (XRD), X-ray photoelectron spectroscopy (XPS), thermogravimetric analysis (TGA), BET analysis, scanning electron

microscopy (SEM), and transmission electron microscopy (TEM). Figure 1A shows the XRD pattern of  $\text{VS}_2/\text{G}$ . The peaks at  $2\theta = 15.38, 32.10, 35.65, 45.25, 57.20, 58.30, 59.63, 64.85,$  and  $69.30^\circ$  are indexed to the (001), (100), (011), (012), (110), (103), (111), (004), and (201) planes, respectively, and they are indicative of pure  $\text{VS}_2$  with no impurities (JCPDS 89-1640). However, an additional peak is found at  $2\theta = 26.60^\circ$ , and it can be indexed to graphene. The XRD results of SG are shown in Figure S2a. The composition and bonding characteristics of  $\text{VS}_2/\text{G}$  were examined by XPS. Figure 1B–D shows the X-ray photoelectron spectra of C1s, S2p, and V2p. The C1s spectrum seen in Figure 1B reveals a C=C signal at a binding energy (BE) of 284.72 eV; the weak signal at a BE of 286.28 eV is indexed to C–OH, and the signal at a BE of 288.80 eV is indexed to the  $\text{O} > \text{C} = > \text{C} - \text{OH}$  group.<sup>[21]</sup> Figure 1C shows the S2p spectrum with two signals at BEs of 162.15 and 163.25 eV in addition to a shake-up satellite at a BE of 167.08 eV. The signal at a BE of 162.15 eV indicates the existence of low-coordination sulfur ions at the surface, and the signal at a BE of 163.25 eV indicates metal bonding to sulfur.<sup>[22]</sup> The V2p spectrum in Figure 1D shows two signals at BEs of 513.38 eV and 520.65 eV, and they can be attributed to the +4 valance state of vanadium.<sup>[19,23]</sup> The XPS chemical composition measurements reveal a 1:1.99 atomic ratio of V/S, which is almost identical to the stoichiometric ratio of  $\text{VS}_2$ . The XPS analysis of SG is shown in Figure S2b,c, and the results indicate the successful introduction of sulfur into the graphene sheets.

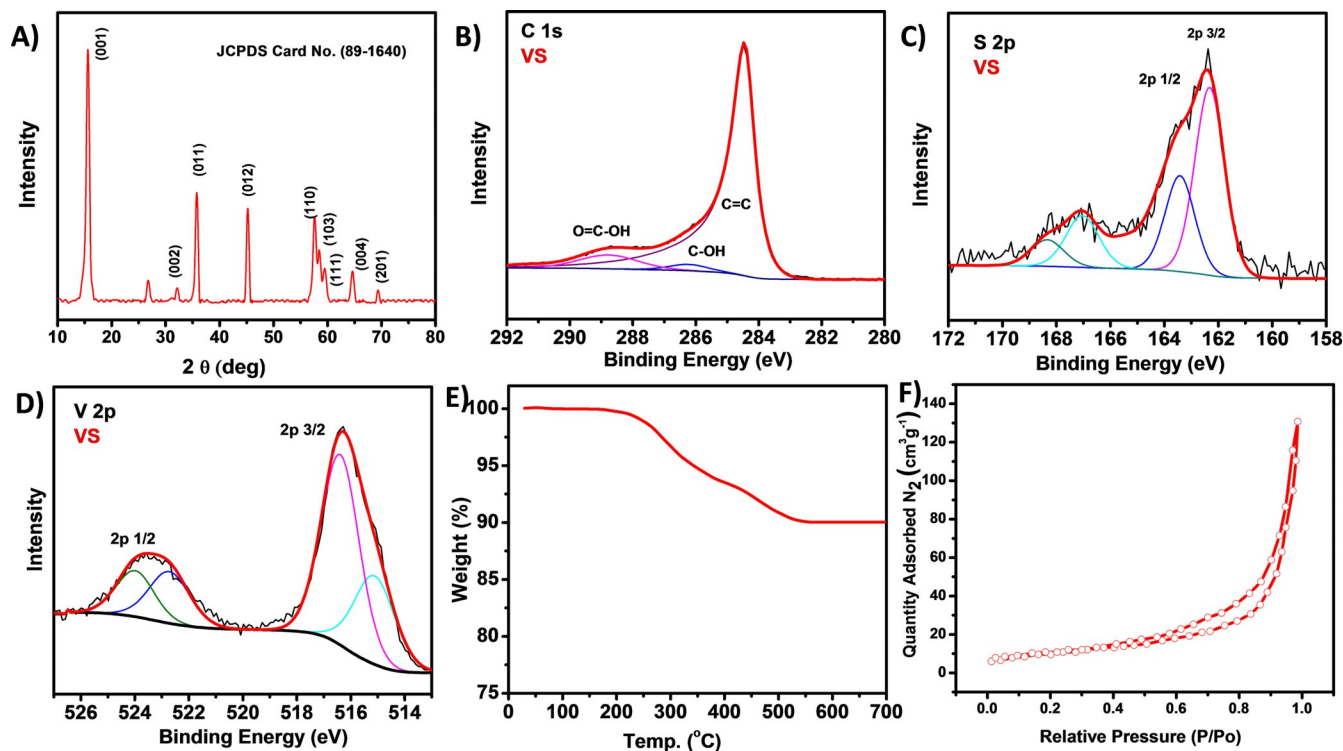


**Figure 1.** A) XRD pattern of  $\text{VS}_2/\text{G}$  showing the standard peaks of  $\text{VS}_2$  (JCPDS 89-1640) with an additional peak at  $2\theta = 26.60^\circ$  indexed to graphene; B–D) X-ray photoelectron spectra of C1s, S2p, and V2p, respectively; E) TGA of  $\text{VS}_2/\text{G}$  showing that  $\text{VS}_2$  comprises 90.1% (wt%) of the material; F) BET analysis showing a type IV  $\text{N}_2$  adsorption–desorption isotherm.



To examine the percentages of  $\text{VS}_2$  and graphene in  $\text{VS}_2/\text{G}$ , TGA was utilized, as shown in Figure 1E. The measurements were performed in air from room temperature up to  $700^\circ\text{C}$  with a ramp rate of  $10^\circ\text{Cmin}^{-1}$ . The results show that  $\text{VS}_2$  comprises 90.10% (wt%) of the material. The BET analysis shown in Figure 1F was conducted by degassing  $\text{VS}_2/\text{G}$  at  $200^\circ\text{C}$  for 2 h under vacuum. The  $\text{N}_2$  adsorption–

desorption isotherm is of type IV with an H3 hysteresis loop,<sup>[24]</sup> and the measured BET surface area is  $32.3\text{ m}^2\text{ g}^{-1}$ .

Figure 2 shows the SEM images of  $\text{VS}_2/\text{G}$ . The flower bouquet-like nanosheet structure of the material is seen in Figure 2A. This morphology allows for a wide contact area between the electrolyte and the material, which leads to a high number of ion-transfer sites and fast charge-transfer kinet-

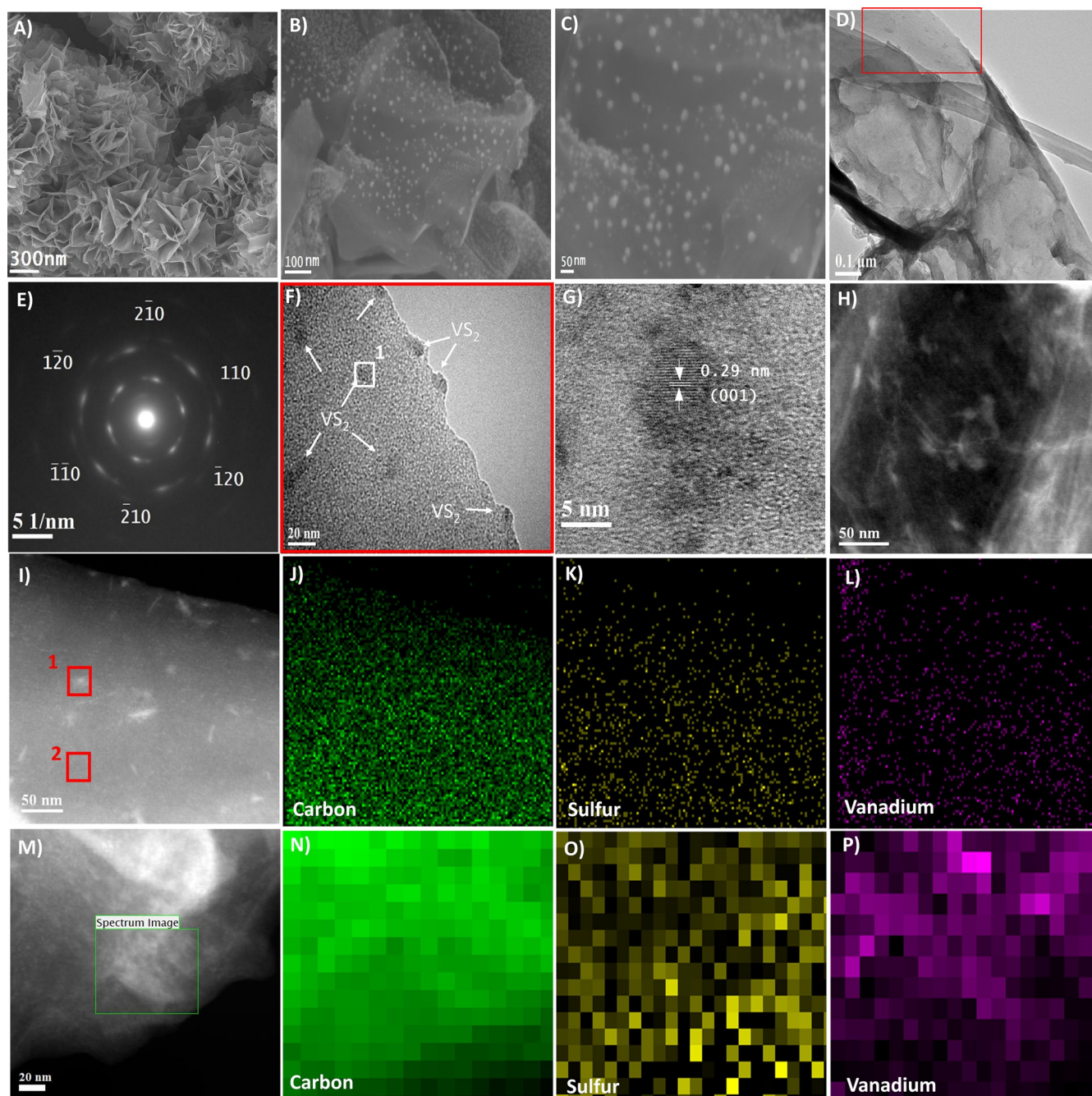


**Figure 2.** A) SEM image of  $\text{VS}_2/\text{G}$  showing the flower bouquet-like nanosheets structure; B) SEM image showing the homogenous distribution of  $\text{VS}_2$  nanoparticles anchored on the surface of the sheets; C) high-magnification SEM image showing small  $\text{VS}_2$  nanoparticles with sizes of 10 to 25 nm; D) low-magnification TEM image showing the  $\text{VS}_2/\text{G}$  sheet-on-sheet with nanoparticles morphology; E) SAD pattern showing the hexagonal symmetry; F) high-magnification HRTEM image of the edge of the image shown in panel d clearly showing small  $\text{VS}_2$  nanoparticles (10–25 nm) on the surface of the sheets; G)  $d$  spacing of the (001) plane; H) HAADF-STEM image showing contrast in brightness between  $\text{VS}_2$  and graphene; I) HAADF-STEM image with elemental quantification on areas 1 and 2; J–L) EDS mapping for carbon, sulfur, and vanadium, respectively; M) EELS investigation area; N–P) EELS mapping of carbon, sulfur, and vanadium, respectively (each pixel is  $4 \times 4\text{ nm}$ ).

ics.<sup>[25]</sup> Figure 2B shows how the VS<sub>2</sub> nanoparticles are anchored on the surface of the sheets with a homogenous distribution without agglomeration. Figure 2C is a higher magnification of the image in Figure 2B, and it shows VS<sub>2</sub> nanoparticles with sizes in the range of 10 to 25 nm. The SEM image of SG is shown in Figure S2d.

The TEM images are shown in Figure 2D–P2d–i. The TEM image in Figure 2D shows the VS<sub>2</sub> sheets on graphene nanosheets morphology with prominent VS<sub>2</sub> nanoparticles adhered to the nanosheets. Figure 2E shows the selected area diffraction (SAD) pattern revealing the typical hexagonal symmetry of the VS<sub>2</sub>/G basal planes.<sup>[20]</sup> Figure 2F is a high-resolution TEM (HRTEM) image of the area selected area in Figure 2D, and it clearly shows VS<sub>2</sub> nanoparticles (10–25 nm) anchored onto the surface of the sheets, which agrees with the SEM findings. Figure 2G shows a lattice spacing of 0.29 nm indexed to the (002) plane. The high-angle annular dark-field scanning transmission electron microscopy (HAADF-STEM) image is shown in Figure 2H. The phase signal (bright field) clearly shows brighter VS<sub>2</sub> nanosheets and nanoparticles on darker graphene sheets, which confirms the sheet-on-sheet structure with prominent nanoparticles. To investigate this further, HAADF-STEM elemental quantification was investigated on area 1 (Figure 2I) containing a prominent nanoparticle and area 2 containing nanosheets (Figure 2I). The results confirm the existence of VS<sub>2</sub> in both areas in a stoichiometric ratio of VS<sub>2</sub>. Energy-dispersive spectroscopy (EDS) analysis was done on the area shown in Figure 2I. The EDS mapping of carbon, sulfur, and vanadium are shown in Figure 2J–L, respectively. The results clearly show the continuous and homogenous distribution of these elements, which further confirms the existence of VS<sub>2</sub> across the whole material structure. The electron energy loss spectroscopy (EELS) technique was used to investigate the elemental distribution at the atomic level. The EELS investigation area is shown in Figure 2M, whereas Figure 2N–P show the EELS mapping of carbon, sulfur, and vanadium, respectively. The results show the harmonized distribution of the elements at the atomic level (each pixel in these images is equivalent to 4 × 4 nm).

The formation of such a unique morphology is influenced by the synthesized material and the reaction conditions described in the Experimental Section in the Supporting Information. Thiourea (TU) is a reducing and allocating agent and anchors to the surface of the graphene oxide (GO) sheets during solvothermal treatment owing to its high dipole moment.<sup>[26]</sup> This leads to the introduction of sulfur into the basal plane of GO simultaneously with its reduction to yield sulfur-doped graphene (SG).<sup>[27]</sup> The introduction of sulfur into the basal plane of graphene is associated with defects.<sup>[26a]</sup> Carbon atoms located on these defects will have higher charge density than the bulk carbon.<sup>[26a]</sup> These sites (containing sulfur and defects) act as nucleation sites for assembly of the vanadium disulfide nanosheets once TU starts to decompose at approximately 190 °C during the solvothermal reaction.<sup>[26b,28]</sup> The morphology of the material suggests that the formation of VS<sub>2</sub> may follow the Volmer–Weber

mode,<sup>[29]</sup> during which the precursors are populated and anchored to the S sites on SG, and over time this leads to the formation of small nanoparticles of VS<sub>2</sub>.<sup>[26b,30]</sup> The particles grow laterally until they eventually coalesce to form continuous sheets of 2D VS<sub>2</sub>, on top of which remains some particles that grow perpendicular to the plane of the 2D sheets of VS<sub>2</sub> as separate islands.<sup>[29a–c,31]</sup> This growth mode has a number of advantages. For example, it hinders the agglomeration of the material and provides a large contact area with the electrolyte; furthermore, it generates strong covalent interactions between VS<sub>2</sub> and the graphene surface, which explains the long cycling stability.

The electrochemical performance was evaluated by using a three-electrode setup and 2 M KOH as the electrolyte. For half-cell measurements, the active material was used as the working electrode, platinum foil was utilized as the counter electrode, and the saturated calomel electrode (SCE) acted as the reference electrode. For full-cell measurements, the working electrode was made of the active material, and the counter electrode was made of an activated carbon/graphene (AC/G) composite. The working electrodes were made by mixing the active material with Super P carbon and polyvinylidene fluoride (PVDF) in a 80:10:10 ratio (wt %). *N*-Methylpyrrolidone (NMP) was used as the solvent to prepare the slurry that was casted (dropwise) on previously cleaned nickel foam (1.5 × 1.5 cm). The electrodes were then dried in a vacuum oven for 12 h before they were pressed under 10 kPa. The mass loading of the working electrodes was approximately 2.10 mg cm<sup>−2</sup>.

Figure 3A shows the cyclic voltammetry (CV) measurements of VS<sub>2</sub>/G at several scan rates in the voltage window of −0.2 to 0.6 V. All curves show two redox peaks, which are indicative of the faradic behavior of the material: the anodic peak results from the oxidation of V<sup>+3</sup> to V<sup>+4</sup>, and the cathodic peak results from the reverse process. Figure 3B shows the galvanostatic charge–discharge measurements at different current densities. All curves show symmetric behavior during the charge and discharge operations; this is indicative of stable charge-transfer kinetics and high stability of the material.<sup>[32]</sup> Notably, all of the discharge curves show similar behavior represented by the voltage drop from 0.5 to approximately 0.35 V, and this can be attributed to a fast non-faradic process (i.e., EDLC). This is followed by a stable decrease in the voltage below 0.35 V until approximately 0.25 V, at which a voltage plateau is noticed; this can be attributed to a relatively slow faradic process. This observation is in agreement with the behavior of the CV measurements. The voltage plateau is seen more clearly at low current densities of 1 and 2 A g<sup>−1</sup> and is less clear at high current densities, which can be attributed to fast reaction transfer kinetics at high current densities.<sup>[33]</sup> The specific capacitance values shown in Figure 3C were obtained from the discharge curves by using Equation (S1).<sup>[10]</sup> A capacitance value of 211 F g<sup>−1</sup> is achieved at a current density of 1 A g<sup>−1</sup>. This superior capacitance is significantly higher than that previously reported in the literature.<sup>[18a,19]</sup> The capacitance maintains 96 % of its value at 1 A g<sup>−1</sup> if the current density is doubled (2 A g<sup>−1</sup>). A



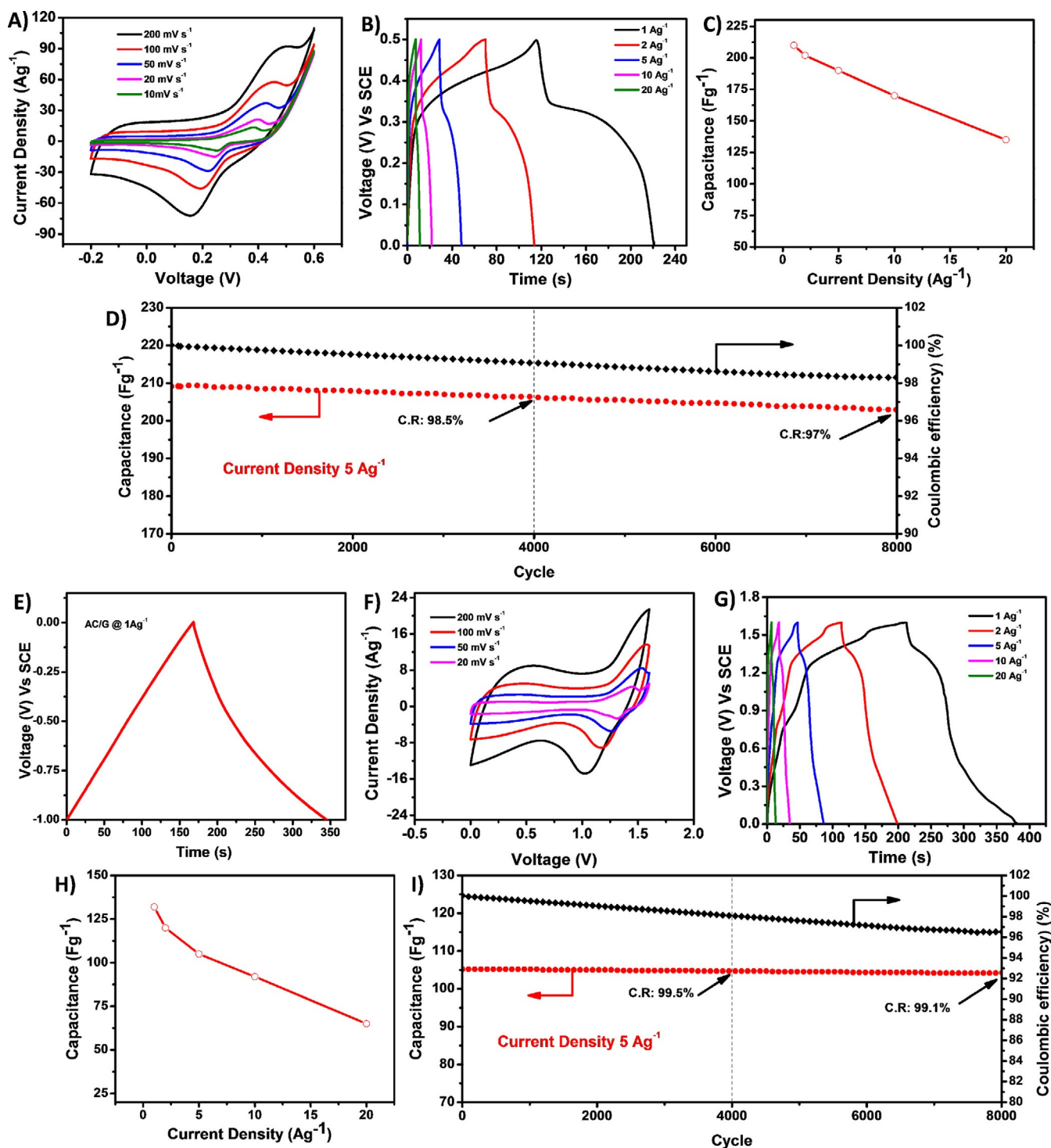


**Figure 3.** A) CV measurements of VS<sub>2</sub>/G at different scan rates, B) charge–discharge measurements at different current densities, C) specific capacitance values, D) long cycling stability test at 5 Ag<sup>-1</sup> for 8000 cycles, E) charge–discharge measurements of the AC/G electrode at 1 Ag<sup>-1</sup>, F) CV measurements of HSC at different scan rates, G) charge–discharge measurements of HSC at different current densities, H) HSC specific capacitance values obtained at different current densities, and I) long cycling test of HSC at 5 Ag<sup>-1</sup> for 8000 cycles.

capacitance retention (CR) of 81 % is achieved, even if the current density is increased to 10 Ag<sup>-1</sup>, and a CR of 64 % is achieved at a current density of 20 Ag<sup>-1</sup>.

A long cycling stability test was performed at 5 Ag<sup>-1</sup> for 8000 cycles, as shown in Figure 3D. The results reveal re-

markable stability with a CR of 98.5 % after 4000 cycles and a CR of 97 % after 8000 cycles. The coulombic efficiencies are 99.2 and 98.5 % after 4000 and 8000 cycles, respectively. These results further confirm the high stability of the material and the excellent reversible reaction kinetics.

These distinguished results can be attributed to the unique morphology of  $\text{VS}_2/\text{G}$ , the use of graphene as a highly conductive substrate, and the presence of nanosized  $\text{VS}_2$  nanoparticles uniformly attached to the sheets. These characteristics lead to an increase in the capacitance owing to an increase in the number of electroactive sites, improved charge-transfer kinetics, and shorter ion-diffusion pathways, all of which result in stable and reversible charge-transfer processes.<sup>[22a,34]</sup>

For further investigation of the electrochemical performance of  $\text{VS}_2/\text{G}$ , we fabricated a hybrid supercapacitor (HSC) by using  $\text{VS}_2/\text{G}$  as the positive electrode and an activated carbon/graphene (AC/G) composite as the negative electrode (AC/G=9:1 wt %); the electrodes were prepared by using the same dropcasting method and weight ratio as those described earlier. The mass ratio of the two electrodes on the sides of the HSC was carefully controlled to balance the charge resulting from the two different charge-transfer kinetics, for which  $\text{VS}_2/\text{G}$  generates charge by using faradic reactions and AC/G generates charge by using an EDLC. The specific capacitance of AC/G was  $168 \text{ F g}^{-1}$ , as calculated from the charge–discharge measurements in Figure 3E. The mass ratio was balanced by using Equations (S2) and (S3).<sup>[35]</sup> The electrochemical performance measurements were done in 2M KOH as the electrolyte and in a wide voltage window of 0–1.6 V, which was determined on the basis of the voltage range of the individual electrodes of the HSC device. Figure 3F shows the CV curve of the HSC at different scan rates. Both battery-like behavior obtained from faradic reactions and standard EDLC behavior can be seen in the CV curves, which indicates simultaneous contribution from both electrodes in the overall capacitance of the HSC device. The behavior of the curves do not change noticeably at all scan rates, and this indicates highly efficient reversible charge exchange processes between the two sides of the HSC and harmonized synergy between the two reaction mechanisms at the cathode and anode.<sup>[36]</sup> Figure 3G shows the galvanostatic charge–discharge measurements of the HSC at several current rates; the curves show symmetric processes of charge gain and release, and both faradic and EDLC behaviors are observed. This further confirms the high synergy between the different reaction mechanisms on both sides of the HSC, which can be attributed to the high stability of the electrodes. The specific capacitance values shown in Figure 3H were calculated by using Equation (S1) on the basis of the total mass of the active material on both electrodes. The HSC shows excellent stability and capacitance retention upon increasing the current density with a CR of 91.0% at a current density of  $2 \text{ A g}^{-1}$  relative to the capacitance observed at  $1 \text{ A g}^{-1}$  and a CR of 51.0% with a 20-fold increase in the current density ( $20 \text{ A g}^{-1}$ ). Figure 3I shows the long cycling test at a current density of  $5 \text{ A g}^{-1}$ . The HSC device shows an outstanding CR of 99.5% after 4000 cycles and a CR of 99.1% even after 8000 cycles relative to the capacitance observed at cycle 1. Electrochemical impedance spectroscopy (EIS) measurements before and after the long cycling are shown in Figure 4A. The Nyquist plot reveals a small change in the solu-

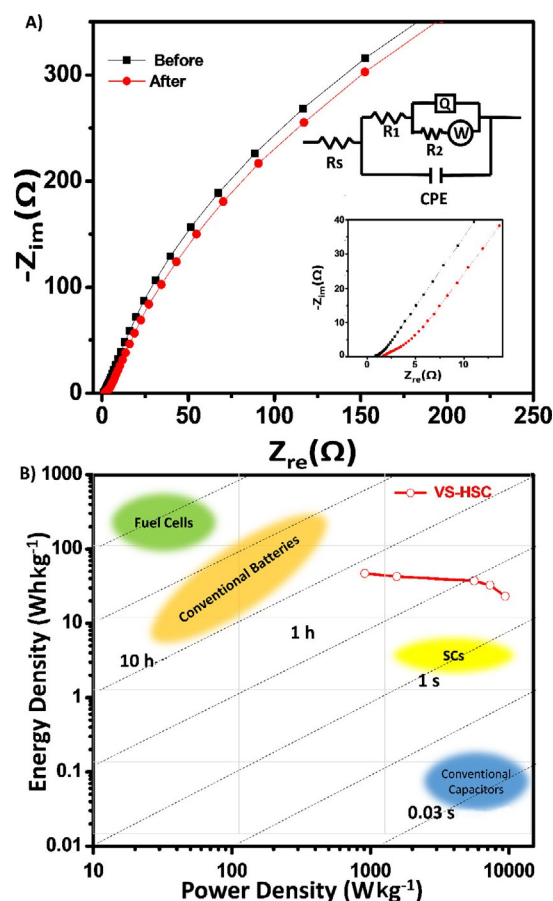


**Figure 4.** A) EIS measurements of the HSC device before and after long cycling with the circuit model shown; the inset shows the low-frequency region in the Nyquist plot used to find  $R_s$  and  $R_{ct}$ . B) Ragone plot of the HSC device.

tion resistance ( $R_s$ ) and charge-transfer resistance ( $R_{ct}$ ) before and after cycling. The  $R_s$  values are  $0.85 \Omega$  before cycling and  $1.55 \Omega$  after long cycling, whereas the  $R_{ct}$  values are  $3.25 \Omega$  before cycling and  $4.75 \Omega$  after cycling. The high slope of the curves in the low-frequency region before and after cycling suggests a small diffusion resistance.<sup>[37]</sup> These results indicate high stability of the HSC device.

Figure 4B shows a Ragone plot of the HSC device. The energy and power densities were obtained by using Equations (S4) and (S5).<sup>[38]</sup> The HSC shows an energy density of  $46.93 \text{ Wh kg}^{-1}$  at a power density of  $0.91 \text{ kW kg}^{-1}$  and retains a high energy density even if the power density is 10 times higher, at which it shows an energy density of  $23.11 \text{ Wh kg}^{-1}$  at a power density of  $9.40 \text{ kW kg}^{-1}$ . This remarkable retention of energy density demonstrates that this material would be ideal for applications requiring a long life and high energy retention at high power rates.

The outstanding electrochemical performance can be ascribed to the inimitable morphology of the material. The 2D nanosheets provide large accessibility of the electrolyte ions and a large number of electroactive sites with short diffusion paths. The 3D nanosized nanoparticles provide excellent ion migration inside the electrode material and high stability.<sup>[39]</sup> This morphology combination and the presence of highly

conductive graphene as the substrate enhance the charge-transfer kinetics, which leads to improved capacitance and faster charge-transfer rates.<sup>[40]</sup>

In conclusion, we successfully synthesized a distinctive flower bouquet-like VS<sub>2</sub> nanosheets structure with small VS<sub>2</sub> nanoparticles (10–25 nm) adhered to it and laying on the surface of graphene nanosheets by using a simple solvothermal process. The material showed superior electrochemical performance with a specific capacitance of 211 F g<sup>-1</sup> at a current density of 1 A g<sup>-1</sup> and superior long cycling performance (8000 cycles) at a current density of 5 A g<sup>-1</sup> with 97% capacitance retention and excellent coulombic efficiency. The material was used to fabricate a hybrid supercapacitor (HSC), which showed outstanding capacitance of 132 F g<sup>-1</sup> at a current density of 1 A g<sup>-1</sup> with remarkable cyclability and capacitance retention. The HSC gave an energy density of 46.93 Wh kg<sup>-1</sup> at a power density of 0.91 kW kg<sup>-1</sup> and an excellent energy density of 23.11 Wh kg<sup>-1</sup> even at a high power density of 9.40 kW kg<sup>-1</sup>. To the best of our knowledge, this is the first report of such a material for HSC applications. This material is a very promising candidate for bridging the gap between battery and supercapacitor technologies.

## Acknowledgements

The authors wish to acknowledge the support provided by the Natural Sciences and Engineering Research Council of Canada (NSERC), the University of Waterloo, and the Waterloo Institute for Nanotechnology.

## Conflict of interest

The authors declare no conflict of interest.

**Keywords:** energy storage • supercapacitors • power density • graphene • vanadium

- [1] a) N.-S. Choi, Z. Chen, S. A. Freunberger, X. Ji, Y.-K. Sun, K. Amine, G. Yushin, L. F. Nazar, J. Cho, P. G. Bruce, *Angew. Chem. Int. Ed.* **2012**, *51*, 9994–10024; *Angew. Chem.* **2012**, *124*, 10134–10166; b) F. M. Hassan, V. Chabot, J. Li, B. K. Kim, L. Ricardez-Sandoval, A. Yu, *J. Mater. Chem. A* **2013**, *1*, 2904–2912; c) C. Wu, J. Maier, Y. Yu, *Adv. Mater.* **2016**, *28*, 174–180.
- [2] M. Armand, J. M. Tarascon, *Nature* **2008**, *451*, 652–657.
- [3] M. R. Lukatskaya, B. Dunn, Y. Gogotsi, *Nat. Commun.* **2016**, *7*, 12647.
- [4] V. Subramanian, S. C. Hall, P. H. Smith, B. Rambabu, *Solid State Ionics* **2004**, *175*, 511–515.
- [5] G. Yu, L. Hu, N. Liu, H. Wang, M. Vosgueritchian, Y. Yang, Y. Cui, Z. Bao, *Nano Lett.* **2011**, *11*, 4438–4442.
- [6] S. Abureden, F. M. Hassan, G. Lui, W. Ahn, S. Sy, A. Yu, Z. Chen, *J. Mater. Chem. A* **2016**, *4*, 12638–12647.
- [7] D. Wei, M. R. J. Scherer, C. Bower, P. Andrew, T. Ryhänen, U. Steiner, *Nano Lett.* **2012**, *12*, 1857–1862.
- [8] X.-C. Dong, H. Xu, X.-W. Wang, Y.-X. Huang, M. B. Chan-Park, H. Zhang, L.-H. Wang, W. Huang, P. Chen, *ACS Nano* **2012**, *6*, 3206–3213.
- [9] a) M. Acerce, D. Voiry, M. Chhowalla, *Nat. Nanotechnol.* **2015**, *10*, 313–318; b) Y.-L. Ding, P. Kopold, K. Hahn, P. A. van Aken, J. Maier, Y. Yu, *Adv. Mater.* **2016**, *28*, 7774–7782.
- [10] S. A. Abureden, F. M. Hassan, G. Lui, S. Sy, R. Batmaz, W. Ahn, A. Yu, Z. Chen, *J. Mater. Chem. A* **2017**, *5*, 7523–7532.
- [11] R. Wang, M. Han, Q. Zhao, Z. Ren, X. Guo, C. Xu, N. Hu, L. Lu, *Sci. Rep.* **2017**, *7*, 44562.
- [12] Y. Huang, H. Li, Z. Wang, M. Zhu, Z. Pei, Q. Xue, Y. Huang, C. Zhi, *Nano Energy* **2016**, *22*, 422–438.
- [13] J. Yan, Q. Wang, T. Wei, Z. Fan, *Adv. Energy Mater.* **2014**, *4*, 1300816.
- [14] a) J. Yang, C. Yu, X. Fan, S. Liang, S. Li, H. Huang, Z. Ling, C. Hao, J. Qiu, *Energy Environ. Sci.* **2016**, *9*, 1299–1307; b) S. Peng, L. Li, C. Li, H. Tan, R. Cai, H. Yu, S. Mhaisalkar, M. Srinivasan, S. Ramakrishna, Q. Yan, *Chem. Commun.* **2013**, *49*, 10178–10180; c) A. Davies, P. Audette, B. Farrow, F. Hassan, Z. Chen, J.-Y. Choi, A. Yu, *J. Phys. Chem. C* **2011**, *115*, 17612–17620.
- [15] a) H. Wang, Y. Liang, T. Mirfakhrai, Z. Chen, H. S. Casalongue, H. Dai, *Nano Res.* **2011**, *4*, 729–736; b) S. Shi, C. Xu, C. Yang, Y. Chen, J. Liu, F. Kang, *Sci. Rep.* **2013**, *3*, 2598.
- [16] a) Y. Liu, R. Wang, X. Yan, *Sci. Rep.* **2015**, *5*, 11095; b) H. Xia, C. Hong, B. Li, B. Zhao, Z. Lin, M. Zheng, S. V. Savilov, S. M. Aldoshin, *Adv. Funct. Mater.* **2015**, *25*, 627–635.
- [17] a) Y. Yan, B. Li, W. Guo, H. Pang, H. Xue, *J. Power Sources* **2016**, *329*, 148–169; b) J. Yuan, J. Wu, W. J. Hardy, P. Loya, M. Lou, Y. Yang, S. Najmaei, M. Jiang, F. Qin, K. Keyshar, H. Ji, W. Gao, J. Bao, J. Kono, D. Natelson, P. M. Ajayan, J. Lou, *Adv. Mater.* **2015**, *27*, 5605–5609.
- [18] a) J. Feng, X. Sun, C. Wu, L. Peng, C. Lin, S. Hu, J. Yang, Y. Xie, *J. Am. Chem. Soc.* **2011**, *133*, 17832–17838; b) H. A. Therese, F. Rocker, A. Reiber, J. Li, M. Stepputat, G. Glasser, U. Kolb, W. Tremel, *Angew. Chem. Int. Ed.* **2005**, *44*, 262–265; *Angew. Chem.* **2005**, *117*, 267–270; c) D. W. Murphy, C. Cros, F. J. Di Salvo, J. V. Waszczak, *Inorg. Chem.* **1977**, *16*, 3027–3031.
- [19] T. M. Masikhwa, F. Barzegar, J. K. Dangbegnon, A. Bello, M. J. Madito, D. Momodu, N. Manyala, *RSC Adv.* **2016**, *6*, 38990–39000.
- [20] X. Sun, T. Yao, Z. Hu, Y. Guo, Q. Liu, S. Wei, C. Wu, *Phys. Chem. Chem. Phys.* **2015**, *17*, 13333–13339.
- [21] G. Beamson, D. Briggs, *J. Chem. Educ.* **1993**, *70*, A25.
- [22] a) S. Khalid, C. Cao, L. Wang, Y. Zhu, *Sci. Rep.* **2016**, *6*, 22699; b) H. Chen, J. Jiang, L. Zhang, H. Wan, T. Qi, D. Xia, *Nanoscale* **2013**, *5*, 8879–8883.
- [23] V. S. Nair, S. Sreejith, P. Borah, S. Hartung, N. Bucher, Y. Zhao, S. Madhavi, *RSC Adv.* **2014**, *4*, 28601–28605.
- [24] K. S. W. Sing, D. H. Everett, R. A. W. Haul, L. Moscou, R. A. Pierotti, J. Rouquerol, T. Siemieniowska, *Handbook of Heterogeneous Catalysis*, Wiley-VCH, Weinheim, **2008**.
- [25] a) Y. Feng, H. Zhang, L. Fang, W. Li, Y. Wang, *J. Mater. Chem. A* **2016**, *4*, 11507–11515; b) N. Parveen, M. H. Cho, *Sci. Rep.* **2016**, *6*, 27318.
- [26] a) F. M. Hassan, R. Batmaz, J. Li, X. Wang, X. Xiao, A. Yu, Z. Chen, *Nat. Commun.* **2015**, *6*, 8597; b) D. C. Higgins, F. M. Hassan, M. H. Seo, J. Y. Choi, M. A. Hoque, D. U. Lee, Z. Chen, *J. Mater. Chem. A* **2015**, *3*, 6340–6350.
- [27] a) S. Pei, H.-M. Cheng, *Carbon* **2012**, *50*, 3210–3228; b) Y. Liu, Y. Li, Y. Yang, Y. Wen, M. Wang, *J. Nanosci. Nanotechnol.* **2011**, *11*, 10082–10086; c) S. Dubin, S. Gilje, K. Wang, V. C. Tung, K. Cha, A. S. Hall, J. Farrar, R. Varshneya, Y. Yang, R. B. Kaner, *ACS Nano* **2010**, *4*, 3845–3852.
- [28] a) Y. Liang, Y. Li, H. Wang, H. Dai, *J. Am. Chem. Soc.* **2013**, *135*, 2013–2036; b) J. Wu, N. Wang, Y. Zhao, L. Jiang, *J. Mater. Chem. A* **2013**, *1*, 7290–7305; c) J. Madarász, G. Pokol, *J. Therm. Anal. Calorim.* **2007**, *88*, 329–336.
- [29] a) S. C. Seel, J. J. Hoyt, E. B. Webb, III, J. A. Zimmerman, *Phys. Rev. B* **2006**, *73*, 245402; b) W. A. Ghanem, F. M. Bayyouni, B. G. Ateya, *Corros. Sci.* **1996**, *38*, 1171–1186; c) D. M. Whelpdale, R. List, *J. Geophys. Res.* **1971**, *76*, 2836–2856; d) V. G. Dubrovskii, *Nucleation Theory and Growth of Nanostructures*, Springer, Berlin, **2014**.
- [30] R. Steudel, *Ind. Eng. Chem. Res.* **1996**, *35*, 1417–1423.
- [31] S. O. Ferreira, S. C. Ferreira, Jr., *Braz. J. Phys.* **2006**, *36*, 294–297.

- [32] M. Rajkumar, C.-T. Hsu, T.-H. Wu, M.-G. Chen, C.-C. Hu, *Prog. Nat. Sci. Mater. Int.* **2015**, 25, 527–544.
- [33] a) M. Krenkel, P. Adelhelm, F. Klein, W. Bensch, *Chem. Commun.* **2015**, 51, 13500–13503; b) S. U. Kim, B. Perdue, C. A. Appleby, V. Srinivasan, *J. Electrochem. Soc.* **2016**, 163, A1535–A1542.
- [34] S. Liu, S. C. Lee, U. M. Patil, C. Ray, K. V. Sankar, K. Zhang, A. Kundu, S. Kang, J. H. Park, S. C. Jun, *J. Mater. Chem. A* **2017**, 5, 4543–4549.
- [35] B. C. Kim, J.-Y. Hong, G. G. Wallace, H. S. Park, *Adv. Energy Mater.* **2015**, 5, 1500959.
- [36] a) L. Shen, J. Wang, G. Xu, H. Li, H. Dou, X. Zhang, *Adv. Energy Mater.* **2015**, 5, 1400977; b) W. Chen, C. Xia, H. N. Alshareef, *ACS Nano* **2014**, 8, 9531–9541.
- [37] Y. Li, F. Tang, R. Wang, C. Wang, J. Liu, *ACS Appl. Mater. Interfaces* **2016**, 8, 30232–30238.
- [38] K. Chen, D. Xue, *ACS Appl. Mater. Interfaces* **2016**, 8, 29522–29528.
- [39] C. Portet, G. Yushin, Y. Gogotsi, *J. Electrochem. Soc.* **2008**, 155, A531–A536.
- [40] a) M. Wagemaker, W. J. H. Borghols, F. M. Mulder, *J. Am. Chem. Soc.* **2007**, 129, 4323–4327; b) L. Kavan, J. Procházka, T. M. Spitler, M. Kalbáč, M. Zúkalová, T. Drezen, M. Grätzel, *J. Electrochem. Soc.* **2003**, 150, A1000–A1007.

---

Manuscript received: April 11, 2017

Revised manuscript received: May 5, 2017

Accepted manuscript online: May 8, 2017

Version of record online: August 9, 2017